Supplementary Information

High thermal conductivities of carbon nanotube films and micro-fibres and their dependence on morphology

Thurid S. Gspann[a,1], Stefan M. Juckes[b], John F. Niven[b], Michel B. Johnson[c], James A. Elliott[a], Mary Anne White[b,c,d], Alan H. Windle[a]

[a] Department of Materials Science and Metallurgy, 27 Charles Babbage Road, University of Cambridge, CB3 0FS, United Kingdom.

[b] Department of Physics and Atmospheric Science, Dalhousie University, Halifax, NS B3H 4R2, Canada.

[c] Institute for Research in Materials, Dalhousie University, Halifax, NS B3H 4R2, Canada.

[d] Department of Chemistry, Dalhousie University, Halifax, NS B3H 4R2, Canada.

S1 – Specific Units

Analogous to specific tensile properties discussed in [1], we use specific electrical and thermal properties to avoid the high uncertainty linked with film thickness or fibre diameters. Both would not only require the use of special equipment such as FIB/SEM or profilometers, but more importantly are intrinsically discrete measurements, while the linear density can be obtained from long lengths of fibre or film and therefore presents a useful average with a much reduced standard deviation. When spun, the fibre itself looks very uniform in density and thickness, and the effect of width change measured in SEM is purely a geometrical folding issue, and can be disregarded if linear density is used.

Symbols:

σ_{el} – electrical conductivity
σ_{el}^{*} – specific electrical conductivity
R – electrical resistance
A – cross-sectional area
L – length between contacts
ρ – density (mass per volume)
κ – thermal conductivity
κ^{*} – specific thermal conductivity
K – thermal conductance
L_m – length of sample weighed
M – mass
LD – linear density (mass per length)

[1] Corresponding author. Tel: +44 (0)1223 334335. E-mail: tsg28@cam.ac.uk (Thurid Gspann)

Specific electrical conductivity

Electrical conductivity, σ_{el}, is related to electrical resistance, R, by $\sigma_{el} = \frac{L}{R \cdot A}$, whereas specific electrical conductivity per density is given by:

$$\sigma_{el}^{*} = \frac{\sigma_{el}}{\rho} = \frac{L}{R \cdot A}\frac{1}{\rho} = \frac{L}{R \cdot A}\frac{L_m A}{M} = \frac{L}{R}\frac{L_m}{M} = \frac{L}{R}\frac{1}{LD}.$$

Note that the cross-sectional area does not change between weighing and attaching contacts for electrical or thermal leads. The length L between the electrical or thermal contacts such as silver paint, however, is by definition shorter than the original total length L_m of the weighed sample.

Using directly the units of the measurements, σ_{el} in [Ω^{-1} mm^{-1}], L in [mm], M in [mg], and total length L_m of weighed sample in [mm], the units of specific electrical conductivity automatically correspond to SI units:

$$\left[\frac{\sigma_{el}}{\rho}\right] = \frac{1}{\frac{\Omega}{mm}}\frac{1}{\frac{mg}{mm}} = \frac{S \cdot m^2}{kg}.$$

In agreement with ([2], [3]), although equivalent to [S m^{-1} g^{-1} cm^3], we use [S m^2 kg^{-1}] to indicate the use of linear density, rather than bulk density and area as the latter would require accurate dimensional measurements.

Specific thermal conductivity

Specific thermal conductivity per density (ρ) is given by $\kappa^{*} = \frac{\kappa}{\rho} = \frac{K \cdot L}{A} \cdot \frac{1}{\rho}$. The cross sectional area A measured is defined as $A = \frac{M}{L_m \rho} = \frac{LD}{\rho}$, with volumetric density ρ, linear density LD, and length L_m of the weighed sample. Hence, the specific conductivity can be rewritten as:

$$\kappa^{*} = \frac{\kappa}{\rho} = \frac{K \cdot L \cdot \rho}{LD} \cdot \frac{1}{\rho} = \frac{K \cdot L}{LD} .$$

We use the units as directly obtained from measurements, A measured in SEM in [µm^2], volumetric density ρ in [g cm^{-3}], length L_m of a weighed sample, linear density LD in [tex = g km^{-1}] and multiply by 10^6. We get the numerical value of specific thermal conductivity in SI units, again sidestepping the necessity for measuring the thickness of films or diameter of fibres, which is the main source for uncertainty in density determination. We will use SI units of [mW K^{-1} m^2 kg^{-1}] which is exactly equivalent to [W m^{-1} K^{-1} (g cm^{-3})$^{-1}$].

$$\left[\frac{\kappa}{\rho}\right] = \frac{W}{m \cdot K}\frac{cm^3}{g} = 10^{-6}\frac{W}{K}\frac{mm}{tex} = \frac{\mathrm{m}W}{K}\frac{m^3}{kg} .$$

S2- CNT samples – Synthesis and Characterisation

Synthesis

Table S1: Spinning parameters for a winding speed 20 m/min.

	Carbon Precursor	Total C precursor input	S:Fe	C:Fe	H_2 flow rate
Type A	Methane	80 ml/min	7.7	1900	0.8 l/min
Type B	Toluene	1.3 g/hr	0.7	400	1 l/min
Type C	n-butanol	2.3 g/hr	0.2	800	1.8 l/min
Type D	n-butanol	3.3 g/hr	0.4	1450	4.5 l/min

Thermogravimetric Analysis

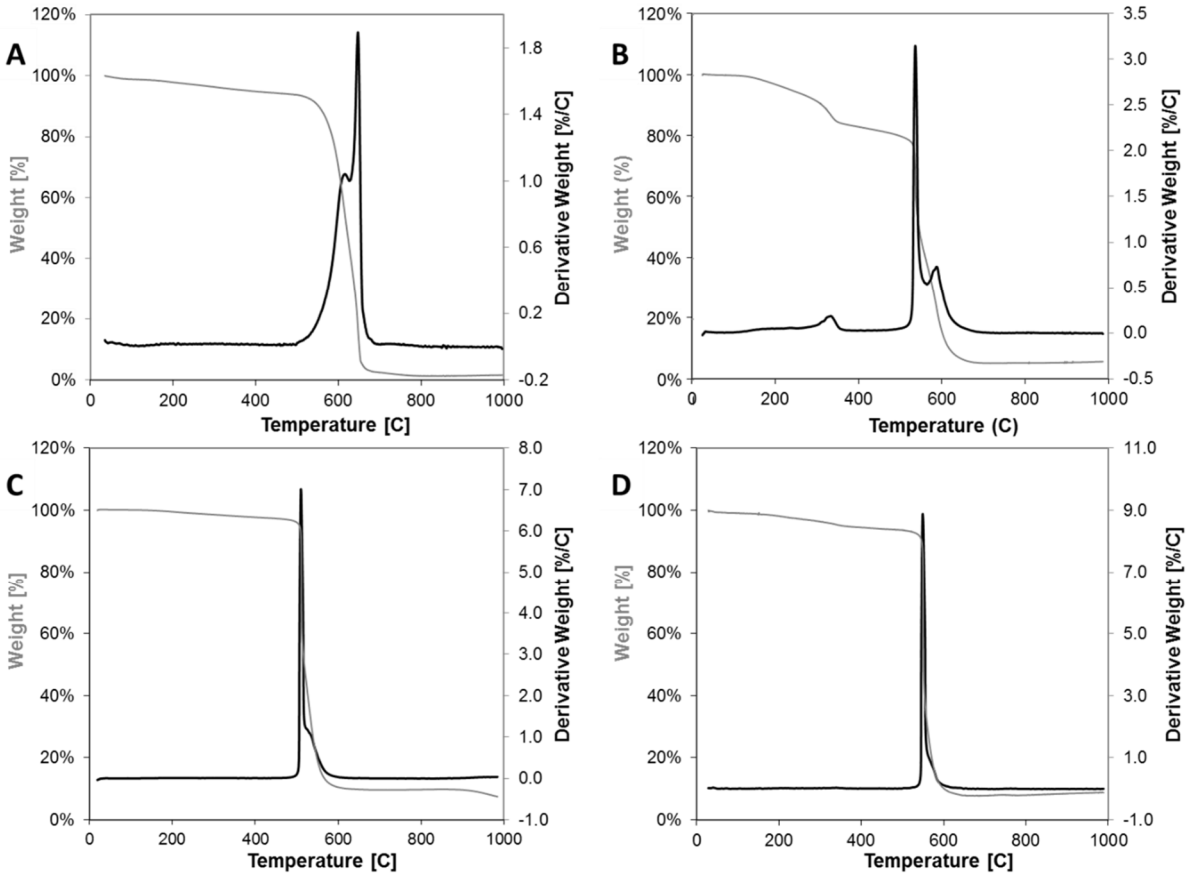

Figure S1: TGA of CNT films spun from methane (A), toluene (C) and n-butanol (C, D).

The samples spun from methane show the lowest residue at 900 °C with 1.3 wt%, followed by toluene with 5% and n-butanol with <10%. The residue gives an estimate for the content of ferrous particles, either inside the CNTs if they served those tubes as catalyst, or as unused nanoparticle impurities. The high burning temperature of the methane sample suggests mainly multi-walled

CNTs, and the shoulders in both Type A and B that there are two main populations comprising the samples. The samples spun from n-butanol show the most abrupt burning event, referring to smallest distribution of CNT wall numbers. High amounts of ferrous nanoparticles in Type C lead to a shift of the main burning event to lower temperatures. Samples A, C and D show mass losses of <6 wt% between 50 and 500 °C, while toluene-spun material shows a clear burning event around 340 °C which relates to the large amount of non-tubular carbon.

Table S2: TGA data analysis.

	Carbon Precursor	Mass Loss <500 °C [wt%]	FeO Residue [wt%]	Main burning event [°C]
Type A	Methane	5.9	1.3	648
Type B	Toluene	20.1	5.2	535
Type C	n-butanol	4.0	9.7	510
Type D	n-butanol	5.7	7.9	549

Transmission Electron Microscopy

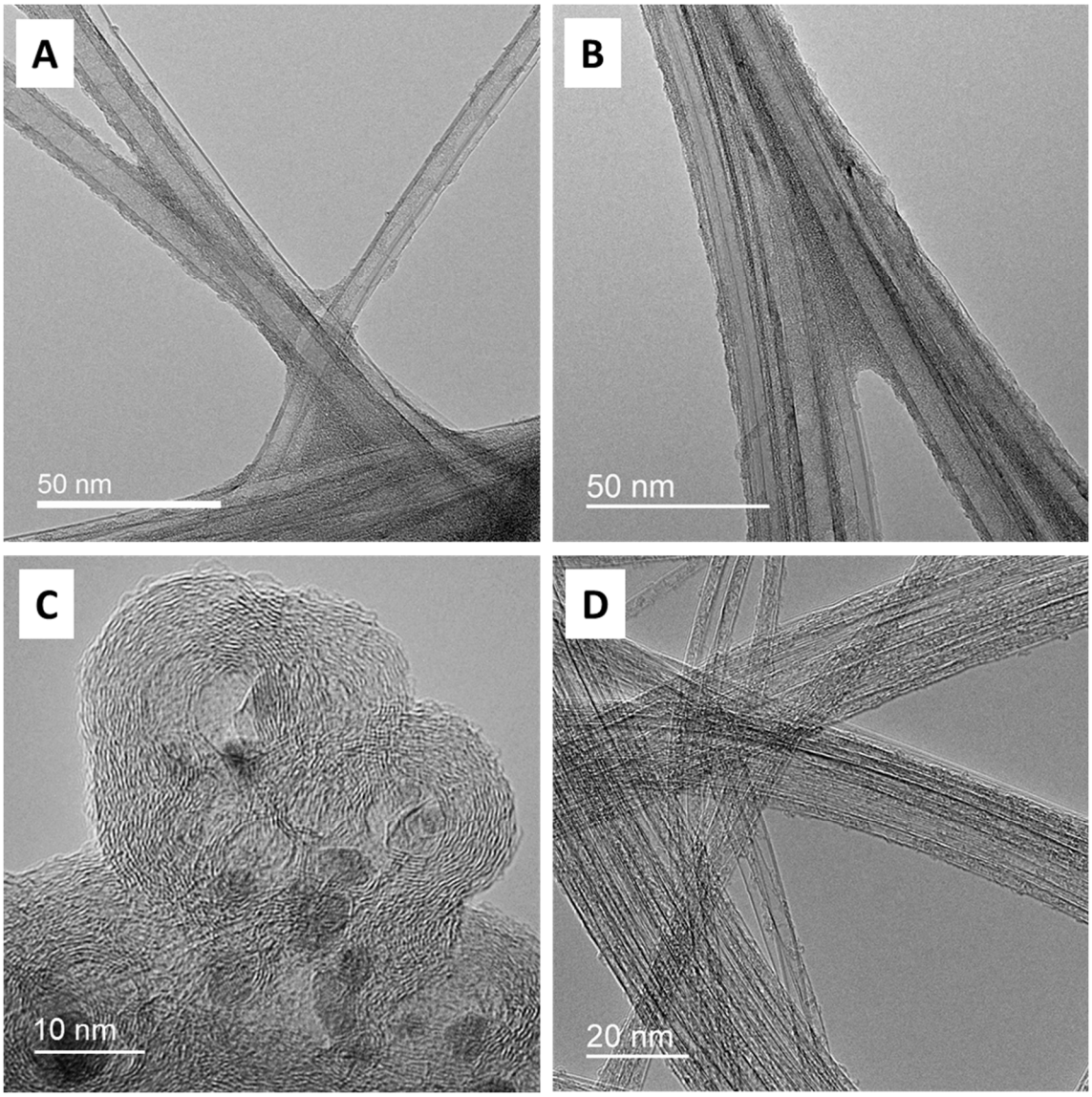

Figure S2: Transmission electron micrographs of CNT samples spun from (A) methane, showing mostly multi-wall CNTs, (B) toluene, showing a mix of few wall tubes which a high amount of carbonaceous coating around the bundles, and (C) and (D) n-butanol: (C) shows a detail of the cluster impurities indicating that large iron particles originated the growth of rather defective multi-wall structures, some of them onion-like. (D) shows the single-wall CNTs covered with only a small amount of amorphous carbon flakes.

Raman

The Raman spectra in Figure S3 were collected with a Bruker Senterra with excitation wavelength 785 nm, 10 mW, 3 seconds integration time, 5 accumulations, depolarized, and averaged from 25 measurement positions per sample. Figure S3 shows the Raman spectra of all four samples collected with 785 nm, 633 nm and 532 nm excitation, at 10 mW, 5 mW and 2 mW, respectively.

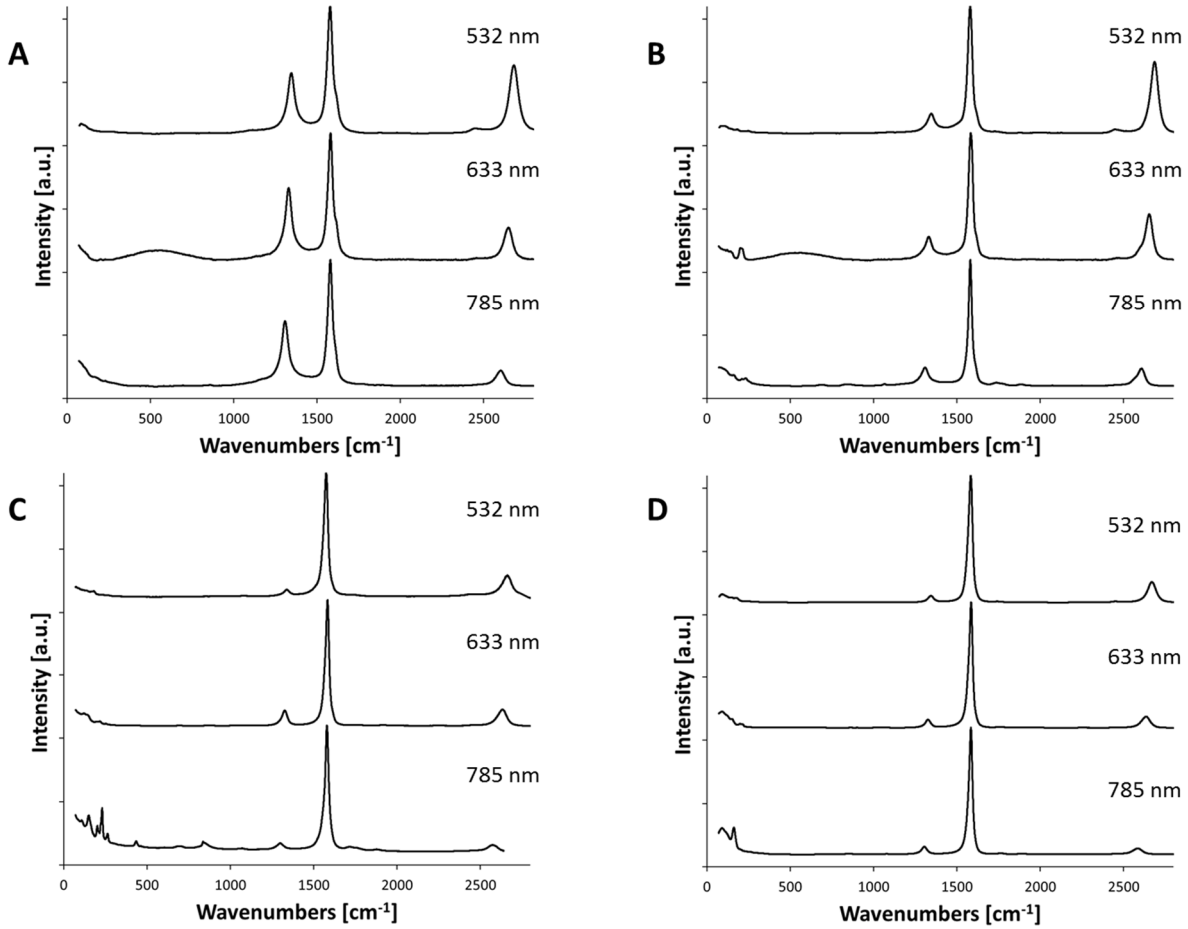

Figure S3: Raman spectra of Type A, B, C and D samples collected at 785 nm, 633 nm, and 532 nm laser excitation wavelength. The presented spectra are averaged from 25 measurement positions which leads to reduction of RBM intensities if the sample is of mixed variety as Type B. Type A shows a ten-fold higher D/G ratio and no RBMs, supporting that the sample is indeed comprised of multi-wall CNTs. Type C and D both show distinct RBMs for the 785 nm spectra, for 633 nm the RBMs are less frequent and loose intensity by the averaging of 25 data points.

The diameters calculated from the radial breathing modes in the averaged Raman spectra are summarised in Table S2, together with the D/G ratios, calculated both from intensity and area. In principle, the use of areal ratios is to be preferred, as the different sources contributing to the D-peak such as multiple walls, defects, ends, or carbonaceous bundle coating have a significant effect

in broadening the peak. Note that we used the raw data for analysis and did not de-convolute the G peak, hence the small contribution from the G* at ~1615 cm^{-1} is included in the G peak area, but regarded as insignificant except for the methane-spun sample, for which the D-peak is so high that the G* influence is again negligible.

Table S3: Raman data analysis from raw data.

	Diameter Range from RBMs [nm]	I_D/I_G (785nm)	A_D/A_G (785nm)	$I_{G_0}/I_{G_{90}}$ (785nm)
Type A	No RBMs, MW	0.53	0.74	4.5
Type B	0.9 – 3.3	0.14	0.28	5.1
Type C	0.9 – 2.5	0.04	0.05	6.7
Type D	0.9 – 3.0	0.05	0.06	7.7

We collected also the Raman spectra in VV and HH configuration, i.e. incident and emitted beam polarized parallel (VV) or perpendicular (HH) to the bundle orientation, to determine alignment from the intensity ratio of the G-peak $I_{G_0}/I_{G_{90}}$. From the SEM images (Figure 2), it is clear that the alignment of the Type D sample is lower than that of Type B. However, considering the Raman data, the G-peak intensity ratio is strongly affected by the amount of carbonaceous bundle coating, which is known to decrease the emitted signal drastically [4]. In case of the n-butanol spun material, the signal is greater by a factor of ~10 than for methane or toluene spun material and so the high $I_{G_0}/I_{G_{90}}$ (Table S3) is a sign of the sample being comprised of clean SWCNTs (i.e. lower background signal), rather than those having better alignment. Hence, for alignment, we employed SEM image analysis and SAXS scans.

CNT bundle alignment: X-ray diffraction

Small angle X-ray scattering (SAXS) was used to determine the orientation of the bundle alignment. Typically, orientation functions for SAXS are determined by the Herman's parameter P_2 which is derived from Legendre polynomials for spherical convolution and is defined as

$$P_2 = \frac{3}{2} < cos^2\chi > -\frac{1}{2}$$

with

$$< cos^2\chi > = \frac{\int I(\chi) \cdot cos^2\chi \cdot sin\chi \, d\chi}{\int I(\chi) \cdot sin\chi \, d\chi}$$

However, it is to be taken into account that $< cos^2\chi >$ defined as above strictly only applies to axially symmetric samples, such as for example crystals or fibres. The films tested here were produced by continusously layering thin films of uncondensed CNT aerogel on top of each other and can be assumed to be layered oriented planes without any orientation in depth. Therefore, we use Chebyshev's polynomial first grade for circular convolution to quantify the orientation [5]. Chebyshev orientation T_2 is defined as

$$T_2 = 2 < cos^2\chi > -1$$

with

$$< cos^2\chi > = \frac{\int I(\chi) \cdot cos^2\chi \, d\chi}{\int I(\chi) \, d\chi}$$

The limiting cases of T_2 are: T_2 = -1 for $< cos^2\chi > = 0$ – alignment perpendicular to the processing direction, T_2 = 0 for $< cos^2\chi > = 1/2$ – unoriented, and T_2 = 1 for $< cos^2\chi > = 1$ – alignment parallel to the processing direction. Table S4 shows the T2 values of the 4 film sample types A, B, C and D.

For the plot in Figure S4, the data were normalized to the maximum intensity of the meridional peak. Insets show the raw XRD diffraction patterns, where the inner circle is dominated by unoriented particles in the samples, therefore, 2θ = 0.0 to 0.3 was excluded from the azimuthal integration. Even so, the expected size range of voids between the bundles, 30 – 150 nm, overlaps with the particle dominated ring. One particular problem with harmonic analysis of orientation is the treatment of the background. If the background is due to scattering from extraneous material such as particles, then it should be discounted. However, if it is due to a completely unoriented fraction of nanotubes, it should be included and would, of course, reduce the orientation coefficient correspondingly. In reality, the background might well be a mix of both components and thus we

have adopted the procedure of fitting Lorentzian peaks to the distribution, to give an estimate of the background to use. Data, Lorentzian fits and the determined background are shown in Figure S4.

Table S4: Analysis of small angle x-ray scattering data.

	T_2
Type A	0.51
Type B	0.63
Type C	0.49
Type D	0.43

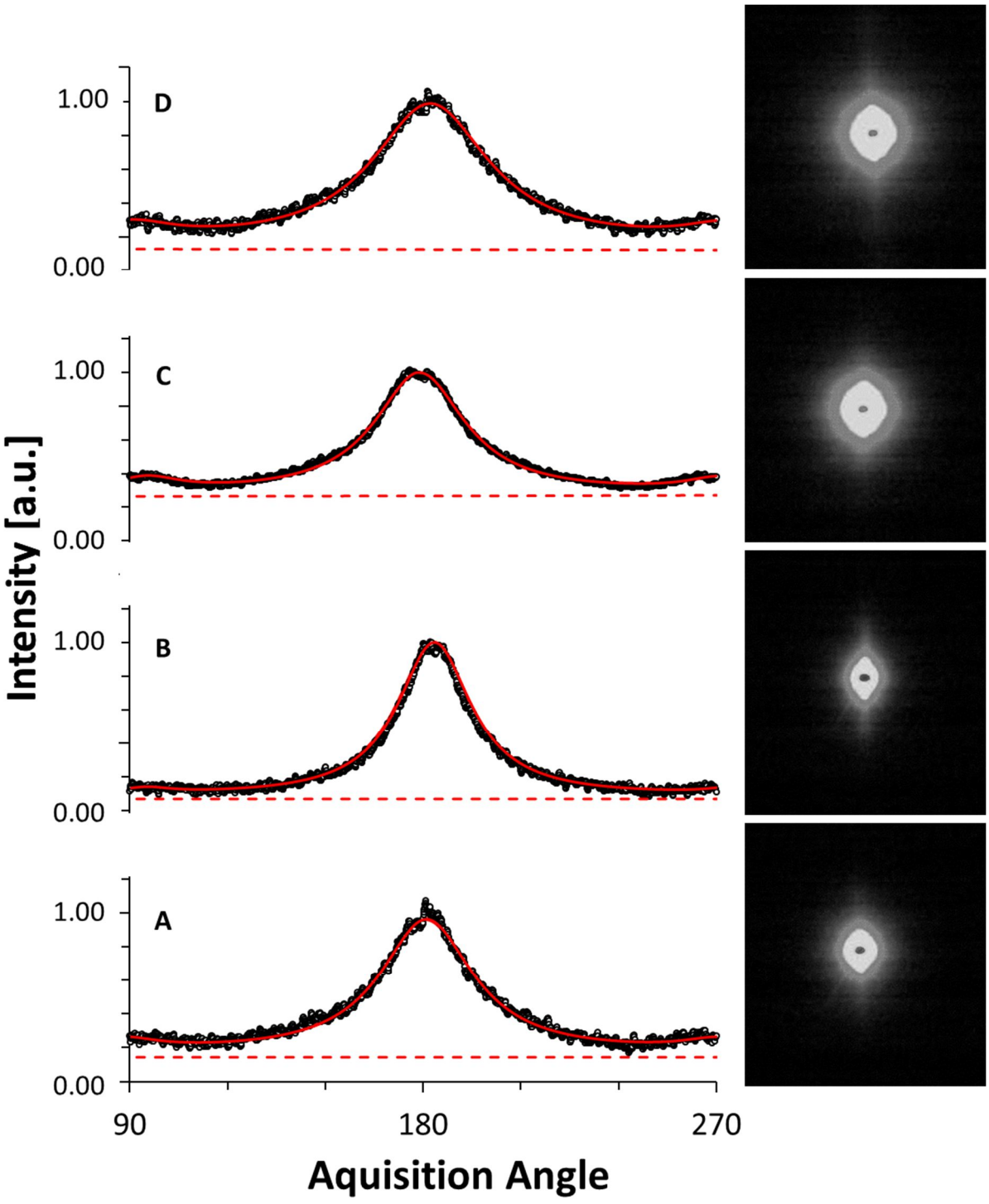

Figure S4: Azimuthal scans of small angle x-ray diffraction patterns, their Lorentzian fits (solid red) and the baselines (dashed red) determined by the fit. The labelling of the graphs corresponds to the film samples Type A, B, C and D. The corresponding diffraction patterns are shown on the right. The data halves for 90 – 270 degrees and 270 – 90 degrees have been averaged, and, for the plot, the curves have been normalized to the maximum intensity.

CNT bundle alignment: FFT analysis from SEM images

The SEM images were analysed by ImageJ software according to the method introduced in [6]. Figure S5 shows the azimuthal scan for the calculation of the first order spherical harmonic coefficient, together with Lorentzian curve fits. Insets show the binary equivalents of the SEM images in Figure 1 and the 2D FFT patterns used for radial integration of pixel intensities.

Intensity ratios of $I_{0°}/I_{90°}$ of the raw data reflect the alignment, the eye observes from the SEM micrographs. Type B shows a three times higher $I_{0°}/I_{90°}$ than Type A, and ten times higher than Type D. $I_{0°}/I_{90°}$ are summarised in table S5, together with the full width at half max (FWHM) of the meridional peak.

SEM images are due to their low focus depth two dimensional and give only little information about order through thickness of a sample. As for SAXS data, we use Chebyshev's polynomial T_2 for quantification. For Types A, B and D, these values reflect the alignment one observes by looking at the SEM images. Type C, comprising aligned CNT bundles and disconnected cluster impurities that appear as if connecting perpendicular to the bundle orientation, result by image analysis in the lowest numerical value for both $I_{0°}/I_{90°}$ and T_2.

Apart from Type C, of which the bundle alignment is better represented by SAXS, the values of T_2 determined by SEM image analysis are in good agreement with T_2 determined by SAXS.

Table S5: 2D FFT data analysis from SEM images.

	$I_{0°}/I_{90°}$	FWHM	T_2
Type A	10.11	0.8	0.51
Type B	31.39	0.5	0.64
Type C	2.80	1.7	0.14
Type D	3.77	0.9	0.42

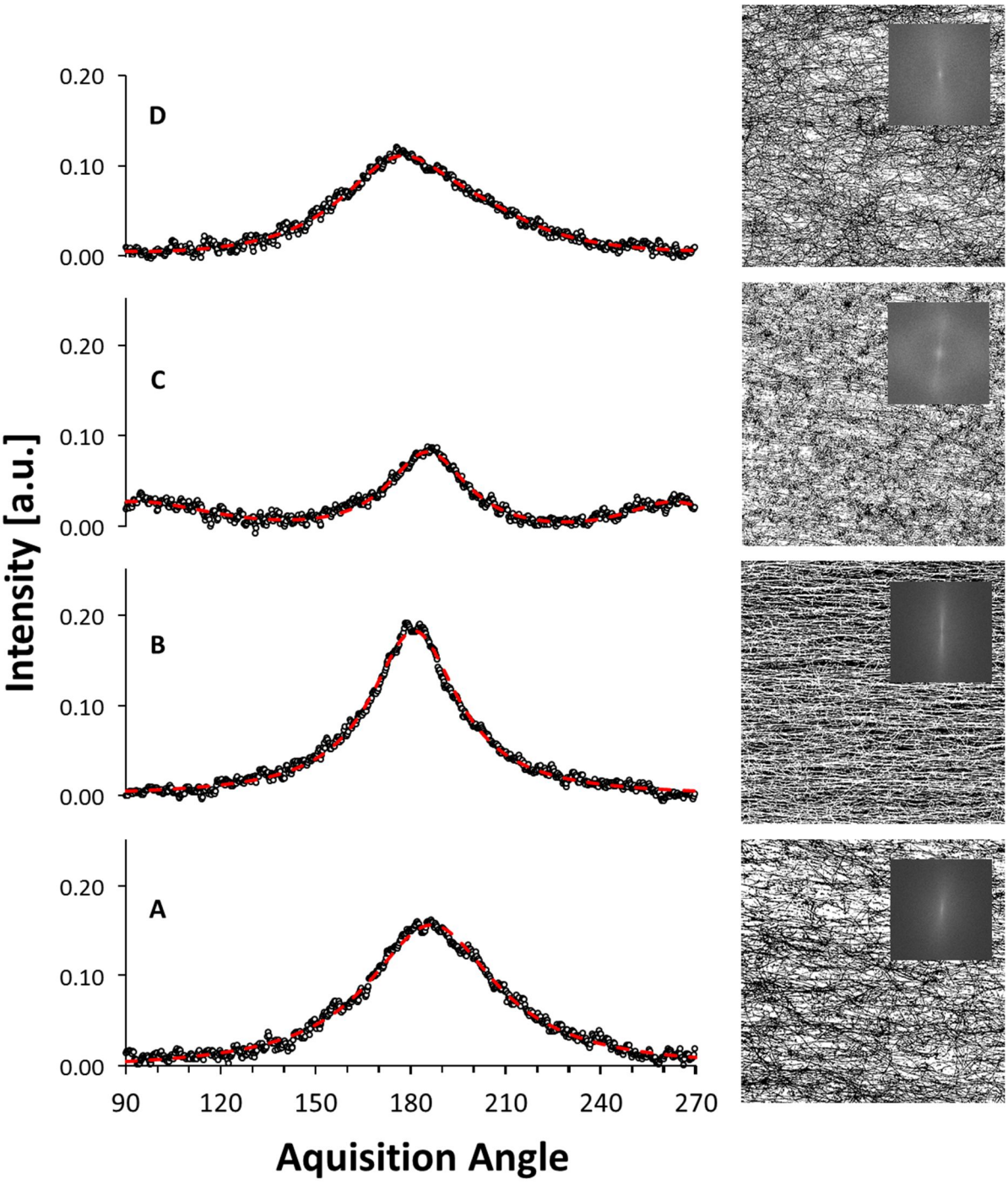

Figure S5: Azimuthal scans of the SEM image 2D FFT analysis and their Lorentzian fits (dashed red) of film samples Type A, B, C and D which corresponds to the labelling of the graphs, with the binary images of the SEMs shown in Figure 1 on the right, and FFT patterns of the azimuthal integration as insets. For the plot, the intensity data were normalized to the minimum intensity.

Mechanical fibre properties

Specific tensile stress over strain of the micro-fibre samples Type A, B and C was tested using a Textechno Favimat tensile tester, with gauge length 20 mm and strain rate 0.1 min^{-1}. Type D samples were not online condensed into fibres. The specific stress and stiffness values are summarized in table S6.

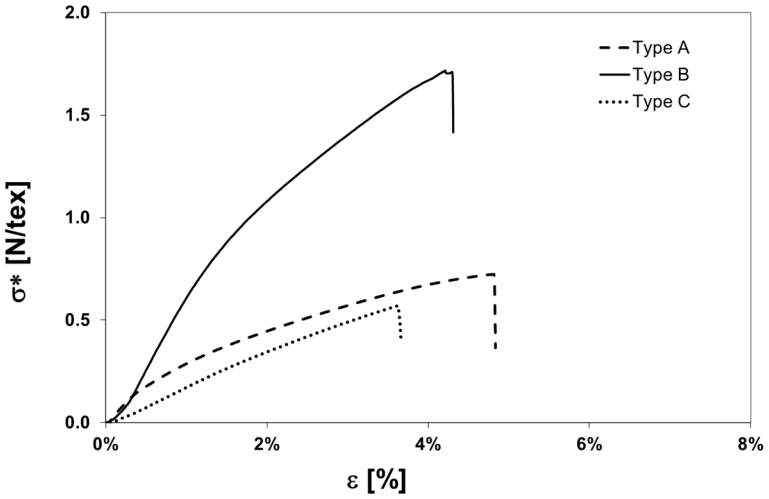

Figure S6: Average curves of specific tensile stress vs strain for fibre samples Type A, B and C.

Table S6: Specific tensile strength σ* and Young's modulus E.

	σ* [N/tex]	E [N/tex]
Type A	0.7 ± 0.1	41.3 ± 3.0
Type B	1.7 ± 0.1	78.0 ± 7.5
Type C	0.6 ± 0.1	24.7 ± 4.2

Sample selection

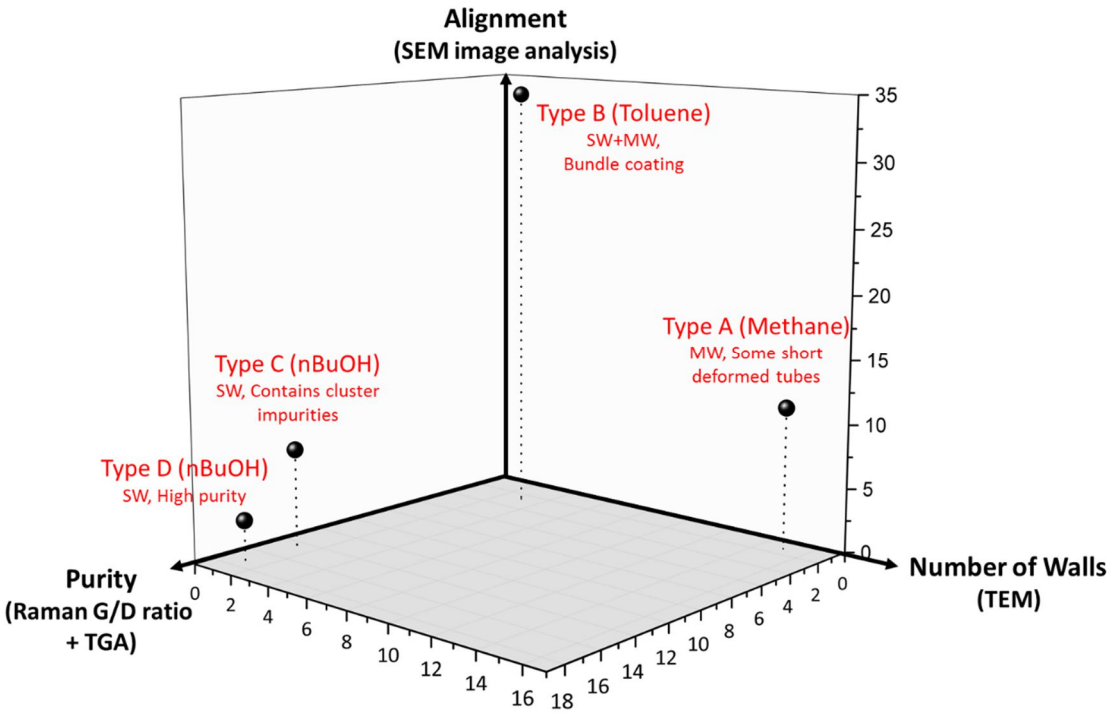

Figure S7: Microstructural parameter space for the samples selection for thermal and electrical conductivity in the style of design of experiment studies. The axes are: purity – using a characteristic parameter calculated as $w \cdot (A_D/A_G)^{-1}$, with w being the carbon content in wt% from TGA, and A_D/A_G being the area D/G ratio from Raman; alignment – obtained as $I_{0°}/I_{90°}$ from 2D FFT image analysis of SEM micrographs; and number of walls as estimated from TEM and Raman, where Raman only provides RBMs as evidence of double- or single wall tubes.

S3- Thermal Conductivity – PTC Sample Stage

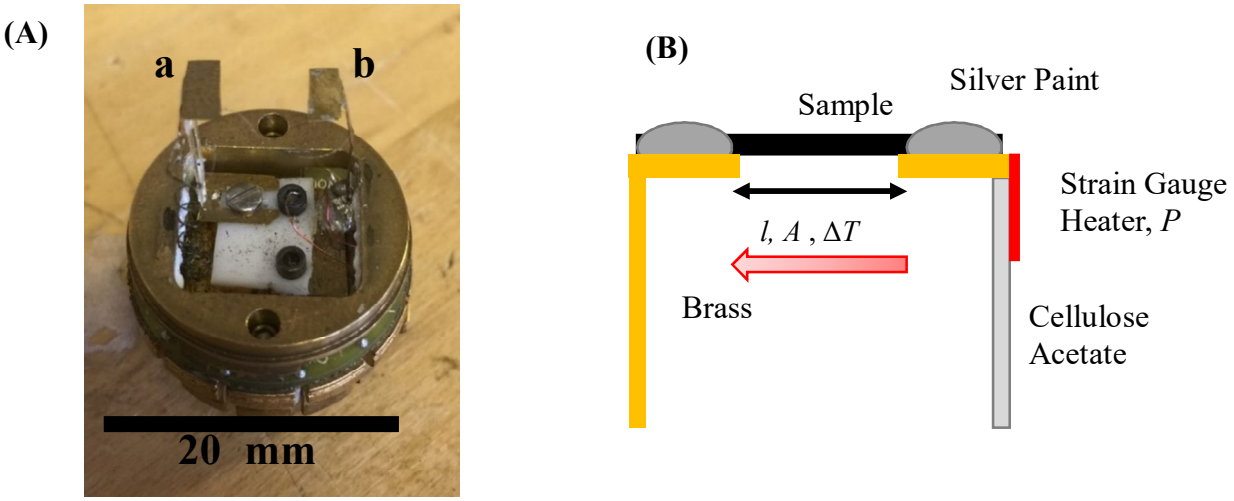

Figure S8: (A) The PTC sample stage, where "a" is the thermally isolated strain gauge heater, and "b" is the heat sink. The distance between the two sample attachments is approximately 6 mm. (B) Schematic illustration of how a sample is attached to the PTC stage. Silver paint was used to minimize the thermal contact resistance, and cellulose acetate was used to isolate the hot side. The red arrow represents the direction of heat flow. A single tape sample is shown attached to both sides.

S4- Individual Measurements of CNT Films

Film thickness measurement

Figure S9 shows the experimental setup for SEM and FIB work. FIB cuts were made using a Hitachi FB-2000A Focused Ion Beam System, while the SEM thickness measurements were done using a Hitachi S-4700 FEG Scanning Electron Microscope. The samples were stored in a sample desiccator between removal of the samples from the FIB and measuring the cross section in the SEM, to minimize sample movement due to ambient air currents. Because the process of FIB milling is very slow, tape samples were pre-split along their length using a scalpel to minimize the distance cut. The thickness of the various tape samples was determined from SEM images using ImageJ software.

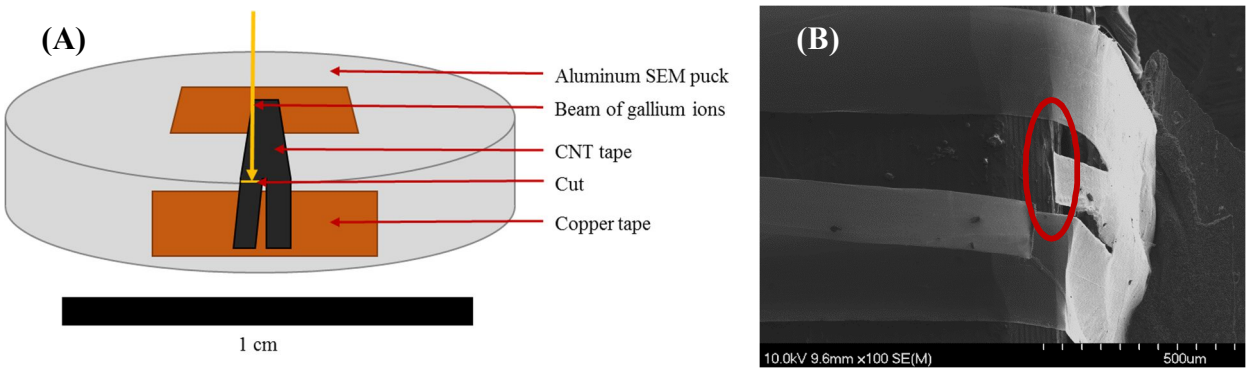

Figure S9: (A) Schematic diagram showing sample mounting technique for FIB cuts. (B) SEM image of a tape (Type D) after a FIB cut was made on the central piece. The region for which thickness was determined is highlighted by the red oval.

The individual measurements of thicknesses of CNT films are presented in Table S7 (samples used for room- temperature electrical conductivity; corresponding specific electrical conductivities in Figure S10), and Table S8 (thermal conductivity). The uncertainties represent the sum of systematic instrument error and random error in the dimension measurement (90% confidence interval, using t-test).

Table S7: Values of dimensions and linear densities, giving electrical conductivity at room temperature after annealing and outgassing of CNT films. Sample length 20 mm and width 1, 2 and 3 mm.

	Width [mm]	Linear density [tex]	Thickness [µm]	σ* [10^3 S m^{-1}]
Type A	0.98 ± 0.02	0.32 ± 0.014	0.093 ± 0.05	34 ± 4
	1.91 ± 0.02	0.60 ± 0.002		64 ± 6
	2.97 ± 0.02	1.07 ± 0.010		74 ± 8
Type B	1.02 ± 0.02	1.08 ± 0.004	3.1 ± 0.4	96 ± 16
	1.95 ± 0.02	2.09 ± 0.002		86 ± 15
	3.17 ± 0.02	2.50 ± 0.010		76 ± 12
Type C	0.73 ± 0.02	0.61 ± 0.002	3.8 ± 0.4	23 ± 5
	1.97 ± 0.02	1.67 ± 0.008		24 ± 3
	2.99 ± 0.02	2.27 ± 0.008		22 ± 3
Type D	0.74 ± 0.02	0.33 ± 0.007	9.8 ± 0.8	7.9 ± 1
	1.17 ± 0.02	0.52 ± 0.030		6.4 ± 1
	2.67 ± 0.02	1.29 ± 0.002		7.1 ± 1

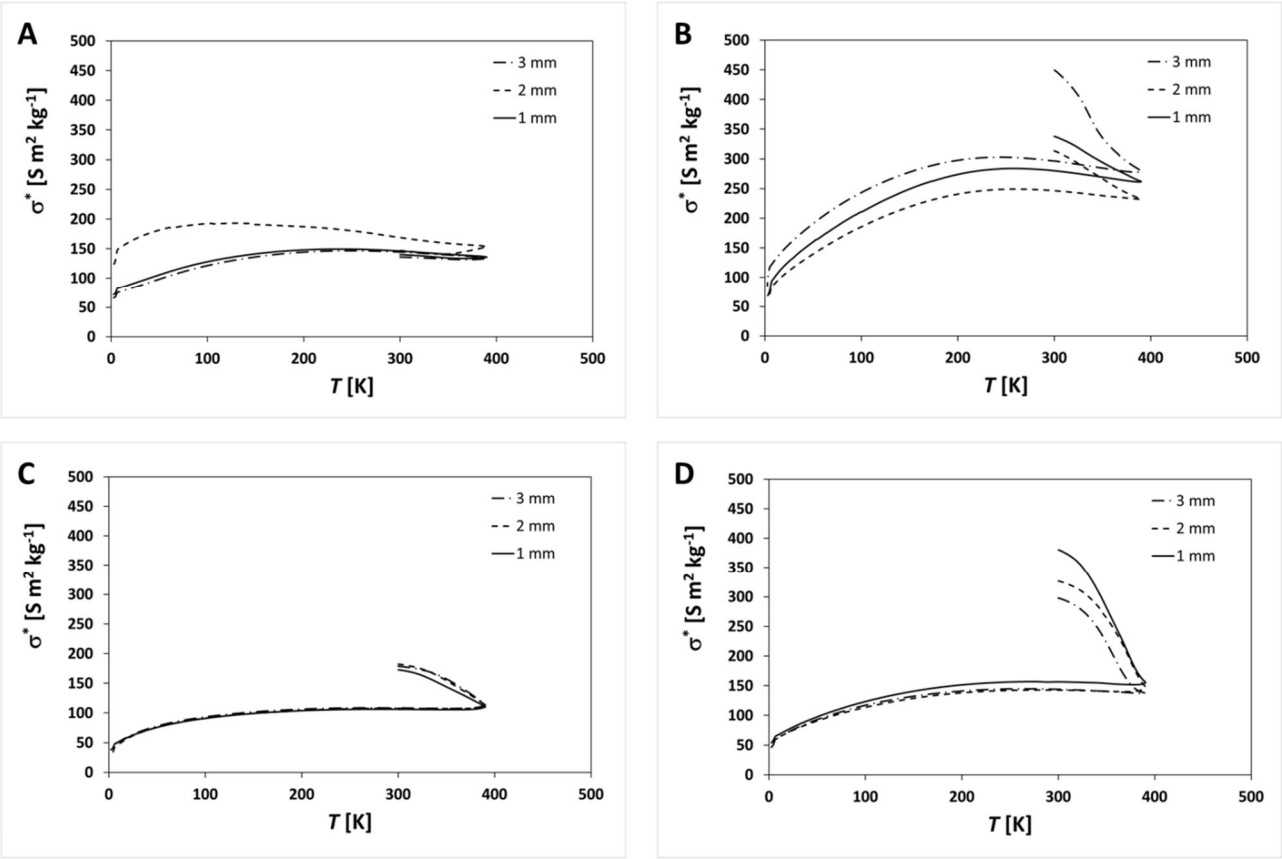

Figure S10: Individual measurements of the specific electrical conductivity vs temperature for 1, 2 and 3 mm film widths. A, B, C and D refer to Type, as described earlier.

Table S8: Values of dimensions and linear densities, giving specific thermal conductivity at room temperature. Thermal conductivity measurements averaged from three specimens per sample type, sample dimensions 3 mm x 12 mm.

	Linear density [tex]	Thickness [μm]	κ (300K) [W m^{-1} K^{-1}]	κ* (300K) [mW K^{-1} m^2 kg^{-1}]
Type A	1.41 ± 0.39	0.93 ± 0.05	110 ± 11	170 ± 5
Type B	3.35 ± 0.65	3.1 ± 0.4	67 ± 12	203 ± 1
Type C	1.76 ± 0.12	3.8 ± 0.4	30 ± 5	185 ± 10
Type D	0.70 ± 0.08	9.8 ± 0.8	7.0 ± 0.9	256 ± 8

S5- Individual Measurements of CNT Fibres

SEM of CNT Micro Fibres

Outside diameters were measured from top views (Figure S11, S12: top rows) and cross sectional areas measured by ImageJ software from FIB cuts (Figure S11, S12: bottom rows). In both cases, assuming circular cross section with the outside diameter would lead to an overestimation of the cross section by more than 70%.

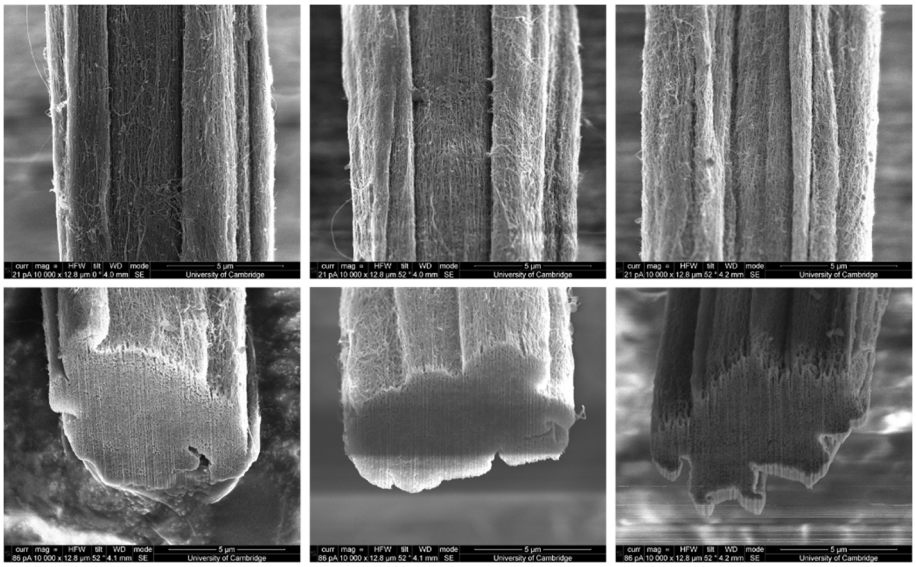

Figure S11: Type A micro-fibre shows outside diameters of 9.85 ± 0.25 µm, but true cross sectional areas of only 39 ± 2 µm². Estimated from three measurement positions each.

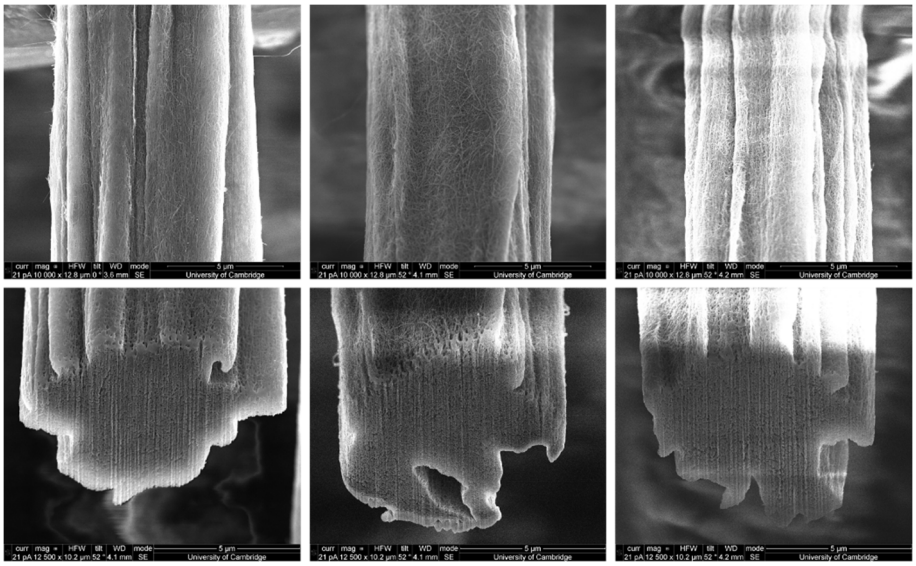

Figure S12: Type B micro-fibre shows outside diameters of 8.2 ± 0.9 µm, but cross sectional areas of only 31.4 ± 0.5 µm². Estimated from three measurement positions each.

Table S9: Dimensional measurements and specific thermal conductivity results at T = 300 K for micro-fibres presented in Figures 13 and 14.

	Linear Density [tex]	Area [μm²]	κ (300K) [W m^{-1} K^{-1}]	κ* (300K) [mW K^{-1} m² kg^{-1}]
Type A	0.025 ± 0.001	38.8 ± 1.9	630 ± 30	970 ± 50
Type B	0.020 ± 0.001	31.5 ± 0.5	770 ± 10	1220 ± 40

S6- Thermal conductivity comparison with literature

Thermal conductivity of CNTs is often reported in absolute terms, usually using the outside fibre diameter to calculate the cross sectional area, which is perfectly valid if the fibres are produced by any kind of twisting. For the fibres in this work, the cross sectional area was calculated from the average of several cross sections cut by focussed ion beam (S5). Similar to Figure 7, Figure S13s compares thermal conductivity with other reported values but includes those for which specific thermal conductivity could not be calculated due to lack of density reported data.

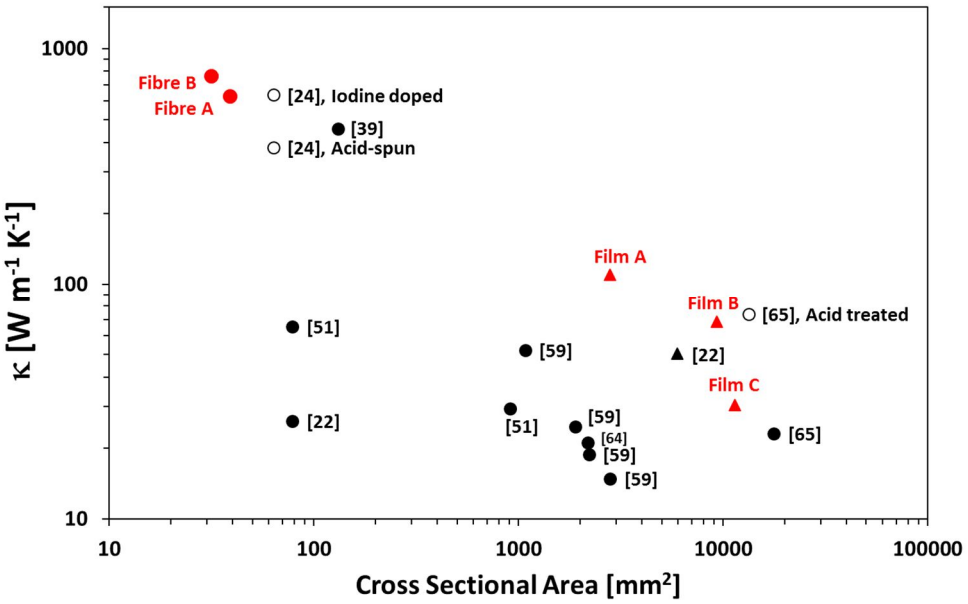

Figure S13: Room-temperature thermal conductivity as a function of cross sectional area, containing additional data points for which density or linear density were not available to calculate specific values (as presented in Figure 7). Black circles and triangles refer to pristine CNT fibres or films, respectively, while open circles refer to treated CNT fibres, such as acid treated or iodine doped. Red circles and triangles refer to the fibres and films presented in this work.

References

[1] K. Koziol, J. Vilatela, A. Moisala, M. Motta, P. Cunniff, M. Sennett and A. Windle, "High-Performance Carbon Nanotube Fiber," *Science,* vol. 318, no. 5858, p. 1892–1895, 2007.

[2] N. Behabtu, C. C. Young, D. E. Tsentalovich, O. Kleinerman, X. Wang, A. W. K. Ma, E. A. Bengio, R. F. t. Waarbeek, J. J. d. Jong, R. E. Hoogerwerf, S. B. Fairchild, J. B. Ferguson, B. Maruyama, J. Kono, Y. Talmon, Y. Cohen, M. J. Otto and M. Pasquali., "Strong, Light, Multifunctional Fibers of Carbon Nanotubes with Ultrahigh Conductivity," *Science,* vol. 339, no. 6116, p. 182–186, 2013.

[3] P. Liu, Z. Fan, A. Mikhalchan, T. Q. Tran, D. Jewell, H. M. Duong and A. M. Marconnet, "Continuous carbon nanotube-based fibers and films for applications requiring enhanced heat dissipation," *ACS Applied Materials & Interfaces,* vol. 8, p. 17461–17471, 2016.

[4] Y. Miyata, K. Mizuno and H. Kataura, "Purity and defect characterization of single-wall carbon nanotubes using raman spectroscopy," *Journal of Nanomaterials,* p. 786763, 2011.

[5] A. Broadhurst, K. Rogers, T. Lowe and D. Lane, "The direct determination of X-ray diffraction data from specific depth," *International Centre for Diffraction Data , Advances in X-ray Analysis,* vol. 48, pp. 183-193, 2005.

[6] A. Mikhalchan, T. Gspann and A. Windle, "Aligned carbon nanotube–epoxy composites: the effect of nanotube organization on strength, stiffness, and toughness," *Journal of Materials Science,* vol. 51, pp. 10005-10025, 2016.